ADVANCED ENERGY MATERIALS
www.advenergymat.de

# Efficient and Effective Synthesis of $CaV_6O_{16}\cdot 2.7H_2O$ as High-Performance Cathode Material for Aqueous Zinc Metal Batteries

*Mengyao Li, Xu Liu, Juan Wu, Xu Dong,* Yude Wang,* and Stefano Passerini**

**Vanadium oxide-based materials are considered to be among the most promising positive electrode candidates for aqueous zinc-metal batteries (AZMBs). However, complex processes, high costs, and insufficient yields of their preparation methods limit further application. Herein, an efficient and effective oil bath method is presented for the preparation of $CaV_6O_{16}\cdot 2.7H_2O$ (CaVO), offering promising performance as cathode material for AZMBs. With commercial crystalline $V_2O_5$, $Ca(CH_3COO)_2$, and water as raw materials, phase-pure CaVO with 42.8 g per batch and a yield of 98.8% can be obtained through the reaction at 90 °C for 6 h. It is further demonstrated that the pre-intercalated $Ca^{2+}$ and $H_2O$ not only expand the interlayer spacing from 4.38 Å for $V_2O_5$ to 8.21 Å for CaVO but also stabilize the interlayer structure of vanadium oxides, promoting the reversibility of CaVO toward the de-/intercalation of $Zn^{2+}/H^+$. In addition, density-functional theory calculations show that the introduction of $Ca^{2+}$ and $H_2O$ effectively improves the diffusion kinetics of $Zn^{2+}$ in CaVO. As a result, CaVO provides high specific capacity (379 mAh $g^{-1}$ at 0.05 A $g^{-1}$) and promising long-term cyclability (94.4% capacity retention after 2200 cycles at 1 A $g^{-1}$), demonstrating the efficient and effective synthesis of vanadium oxide-based cathode materials for high-performance AZMBs.**

## 1. Introduction

As fossil fuel scarcity and environmental pollution increase, more and more countries are committing to the goal of carbon neutrality.[1] The development and utilization of renewable and clean energy sources such as solar and wind are keys to achieving carbon neutrality.[2] However, these renewable sources are intermittent and unstable, which leads to the urgent development of efficient energy storage devices to store the generated power. In recent years, aqueous zinc metal batteries have attracted increasing attention due to their high safety, low cost, and impressive electrochemical performance, expected to be used in large-scale stationary energy storage.[3]

Cathode materials are an important component determining the electrochemical performance of AZMBs. A large number of electrode materials with different crystal structures, chemical compositions, and morphologies have been reported, including vanadium-based oxides,[4] manganese-based oxides,[5] Prussian blue analogs,[6] organic compounds,[7] and some other materials. Among them, vanadium-based materials with multiple valence states (from +2 to +5) and open crystal structures, promising high theoretical capacity and rate capability, have attracted much attention.[8] However, the strong electrostatic interaction between $Zn^{2+}$ and $V_2O_5$ still limits the diffusion kinetics of $Zn^{2+}$ and the repeated de-/intercalation of $Zn^{2+}$ results in structural collapse and rapid capacity degradation.[9]

M. Li, J. Wu, Y. Wang
National Center for International Research on Photoelectric and Energy Materials
School of Materials and Energy
Yunnan University
Kunming 650504, China
E-mail: ydwang@ynu.edu.cn

X. Liu, X. Dong, S. Passerini
Helmholtz Institute Ulm (HIU)
Helmholtzstrasse 11, 89081 Ulm, Germany
E-mail: xu.dong@kit.edu; stefano.passerini@kit.edu

X. Liu, X. Dong, S. Passerini
Karlsruhe Institute of Technology (KIT)
PO Box 3640, 76021 Karlsruhe, Germany

Y. Wang
Yunnan Key Laboratory of Carbon Neutrality and Green Low-Carbon Technologies
Yunnan University
Kunming 650504, China

S. Passerini
Austrian Institute of Technology (AIT) Transport Technologies
Giefinggasse 4, Wien 1020, Austria

The ORCID identification number(s) for the author(s) of this article can be found under https://doi.org/10.1002/aenm.202404037



**DOI: 10.1002/aenm.202404037**

Various efforts have been made to solve these problems. For example, pre-inserting dopants are considered a feasible method to expand the interlayer spacing of vanadium oxides, which, consequently, improves the diffusion kinetics of $Zn^{2+}$ and the structural stability.[10] In 2016, Kundu et al.[11] reported for the first time a $Zn_{0.25}V_2O_5{\cdot}nH_2O$ layered material with $Zn^{2+}$ pillaring the V-O slabs as the cathode material for aqueous zinc metal batteries. The large interlayer spacing and nanobelt morphology with a high aspect ratio provide channels for the transport of $Zn^{2+}$ and electrons, respectively. Here, the $Zn^{2+}$ ions act as pillars, stabilizing the interlayer structure and enabling a high specific capacity of 300 mAh $g^{-1}$ with a remarkable capacity retention of 80% after 1000 cycles. Since then, various metal and non-metallic ions ($Li^+$, $Na^+$, $K^+$, $NH_4^+$, $Ba^{2+}$, $Mg^{2+}$, $Cu^{2+}$, $Al^{3+}$, etc.) have been pre-intercalated into the interlayer of vanadium oxides, effectively mitigating the interlayer sliding and structural collapse issues.[12] In addition, it was also found that structural $H_2O$ molecules in the interlayer have a significant effect on improving the diffusion kinetics of $Zn^{2+}$. Yan et al.[13] systematically investigated the chemical composition and crystal structure evolution of the $V_2O_5{\cdot}nH_2O$ cathode during dis-/charge. The results show that the presence of structured water can reduce the effective charge of $Zn^{2+}$, thus reducing the electrostatic interactions between $Zn^{2+}$ and $V_2O_5$, which is favorable for the reversible de-/intercalation of $Zn^{2+}$.

Despite this progress, previous studies mainly focused on the electrochemical properties of materials themselves, overlooking the difficulty of their synthesis methods for practical applications. The practical application of vanadium-based materials is limited by the lack of an effective and efficient synthesis with high yield. Most of the vanadium-based oxide materials reported to date for aqueous zinc batteries are prepared via hydrothermal, sol-gel, and solid-phase sintering methods.[14] Although the prepared vanadium-based oxide cathodes exhibit excellent electrochemical properties, the drawbacks of these methods cannot be ignored. The solid-phase sintering method is feasible for scaling up preparation of vanadium oxides in a few hours, but the high-temperature sintering process increases energy consumption and adds higher requirements on equipment.[15] Moreover, sintering temperatures above 350 °C remove the water molecules in the interlayer spacing, reducing the interlayer distance. The sol-gel method allows the synthesis of hydrate vanadium oxides with fine nano-/microstructure at room temperature, but the preparation process requires multiple steps and, particularly, a long synthesis time of up to several days.[16] Hydrothermal methods well balancing the reaction duration and reaction temperature have been the most commonly adopted methods to prepare vanadium oxide-based materials. Nonetheless, reaction temperatures above 100 °C and, consequently, high pressure, together with a reaction duration of tens of hours, still raise concerns about safety and large-scale production.[17] In addition, the synthesis of some vanadium-based materials is sensitive to the pH of the solution, which further increases the complexity and difficulty in the preparation of phase-pure materials.[18] Therefore, developing a simple and efficient synthesis process for vanadium-based materials with high performance is a meaningful task.

In this work, we report a mild, low-cost, and high-yield synthesis of $CaV_6O_{16}{\cdot}2.7H_2O$ (CaVO) and explore its energy storage mechanism in aqueous electrolytes. Phase-pure CaVO with 42.8 g per batch and a yield of 98.8% can be obtained via facile oil-bath heating the reactant at 90 °C for 6 h, which offers significant advantages over previous preparation procedures in terms of simplicity, time, and cost. In addition, the CaVO cathode shows high specific capacity and excellent long-term stability due to its large layer spacing and water lubrication effects. Moreover, we confirmed its structural stability during cycling and demonstrated that the introduction of $Ca^{2+}$ and $H_2O$ enhances $Zn^{2+}$ diffusion, improving overall performance.

## 2. Results and Discussion

### 2.1. Structure Characterization

CaVO was synthesized at moderate temperature employing an oil bath and commercial crystalline $V_2O_5$, $Ca(CH_3COO)_2$, and water as raw materials (**Figure 1a**). Upon heating the solution/slurry of the reagents with the oil bath at 90 °C for 6 h, phase-pure CaVO (42.8 g per batch) was obtained with a yield of 98.8%. More information on the experimental procedure can be found in Supporting Information. The crystalline $V_2O_5$ consists of [$VO_5$] square pyramids without any ion or water between the V-O layers. Upon heating, $H_2O$ in the solution attacks the exposed vanadium in [$VO_5$], resulting in partial conversion of [$VO_5$] to [$VO_6$] (see Figure 1a).[17a] As a result, [$VO_5$] tetrahedral cones and [$VO_6$] octahedra, which are co-rimmed with each other, are connected at common angles to form $V_3O_8$ layers aligned along the *c*-axis of CaVO. Meanwhile, the positively charged $Ca^{2+}$ stabilizes the lamellar structure by forming Ca-O bonds with the negatively charged oxygen in the adjacent V-O layer through electrostatic attraction.[19] Therefore, the $H_2O$ molecules and $Ca^{2+}$ distributed in the interlayers not only expand the interlayer spacing from 4.38 Å of pristine $V_2O_5$ (PDF 41–1426) to 8.50 Å of CaVO but also act as pillars stabilizing the layered structure, which is expected to promote the electrochemical performance in AZMBs.

The crystal structure of the sample was characterized by X-ray diffraction (XRD). As shown in Figure 1b, all the diffraction features can be indexed to the corresponding diffraction reflections of $CaV_6O_{16}{\cdot}3H_2O$ (PDF 33–0317). The amount of structural water in the material was further determined by thermogravimetric analysis (TGA) (Figure 1c). The weight loss before 130 °C can be attributed to the water weakly adsorbed on the surface, while the weight loss between 130 and 500 °C is ascribed to the water molecules in the interlayer of the CaVO. Based on the second weight loss, i.e., 7.48 wt.%, the molecular formula of the prepared sample is verified to be $CaV_6O_{16}{\cdot}2.7H_2O$. Figure 1d displays the Raman spectrum of the obtained CaVO. Various features reflecting the local bonds between vanadium and oxygen can be observed, as summarized in Table S1 (Supporting Information). The peak located at 240 $cm^{-1}$ can be assigned to the vibration of the Ca-O bond,[20] demonstrating that $Ca^{2+}$ is successfully introduced into the interlayer and bonding to the terminal oxygen in the V-O layer.

XPS was used to characterize the surface valence state of CaVO. The XPS survey spectrum is displayed in Figure S1(Supporting Information). Besides the C 1s peak commonly originating from contamination, only peaks related to Ca, V, and O are observed. The high-resolution XPS spectrum of O 1s is shown in Figure 1e. The peaks at 530.3, 531.5, and 532.6 eV can

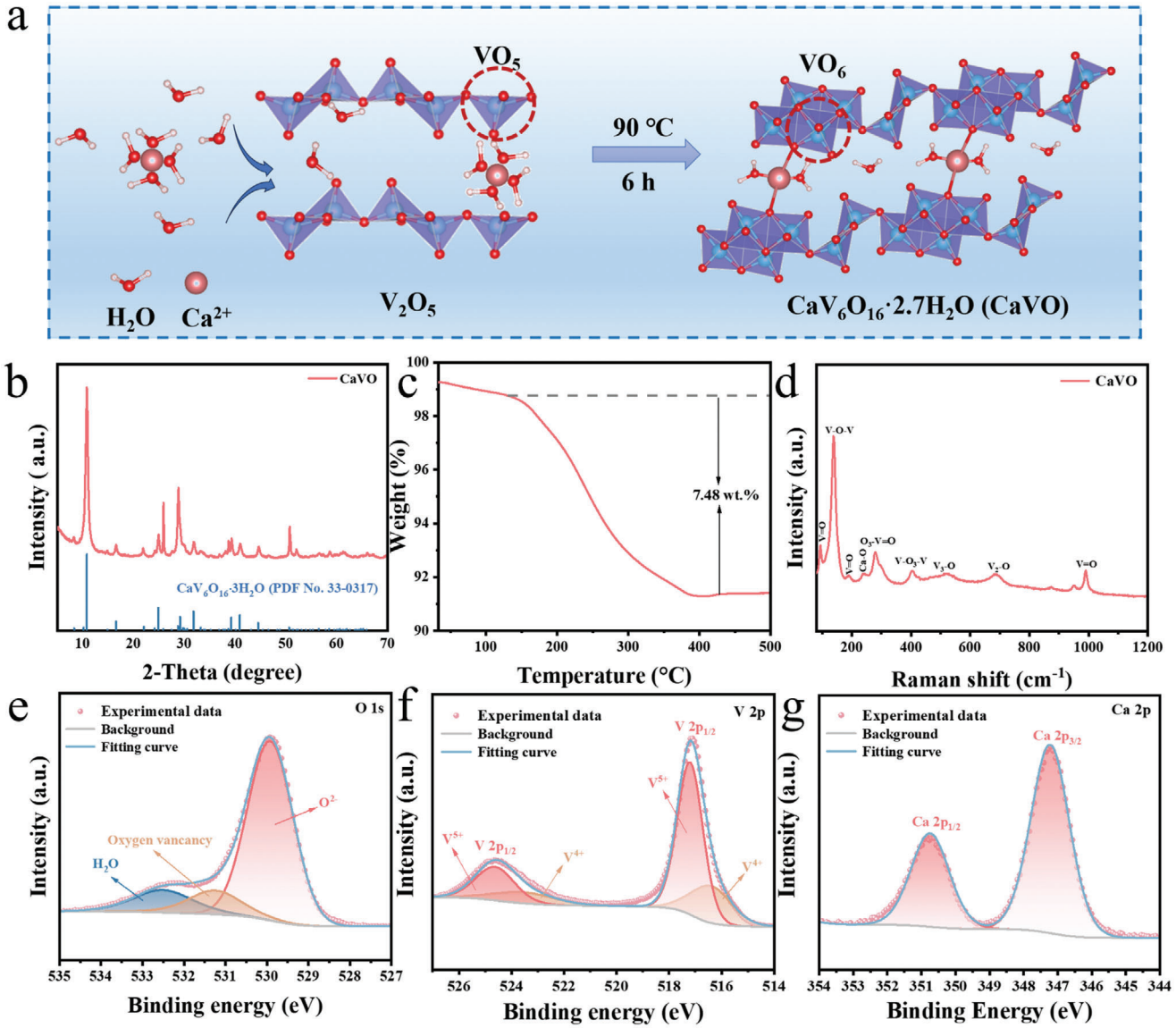


**Figure 1.** a) Schematic diagram of the preparation process as well as the crystal structure of CaVO. b) XRD patterns, c) TAG curves, and d) Raman spectrum of CaVO. High-resolution XPS spectra of e) O1s, f) V 2p, and g) Ca 2p for CaVO.

be indexed as $O^{2-}$, oxygen vacancies, and $H_2O$, respectively. The presence of oxygen vacancies can provide more active sites and regulate the surface adsorption and internal diffusion of $Zn^{2+}$, thereby enhancing ion and charge transfer kinetics.[21] Figure 1f shows the high-resolution XPS spectra of V 2p, in which the peaks at 517.2 and 524.9 eV correspond to V $2p_{3/2}$ and V $2p_{1/2}$ of $V^{5+}$, respectively, while the peaks at 516.3 and 523.9 eV originate from V $2p_{3/2}$ and V $2p_{1/2}$ of $V^{4+}$, respectively. These results suggest that most vanadium has a valence state of +5 and a smaller fraction has a valence state of +4 in the prepared CaVO. The high-resolution XPS spectrum of Ca 2p in Figure 1g demonstrates the presence of $Ca^{2+}$ in the prepared CaVO.

Scanning electron microscopy (SEM) and transmission electron microscopy (TEM) were carried out to explore the morphology and structure of CaVO. As shown in **Figures** 2a,b, and S2 (Supporting Information), the prepared CaVO consists of uniform nanoribbons with a width of ≈100–300 nm and a length of up to several μm. It is worth noting that this nanobelt structure, which extends along a single directional axis, has a natural geometric advantage in ion transport.[22] At the same time, the 1D nanostructure provides a direct pathway for efficient charge transport, which can reduce the diffusion distance of $Zn^{2+}$ and accelerate the transport kinetics in the electrode.[23] TEM images (Figure 2c) also confirm that CaVO consists of ultrathin nanoribbons. The high-resolution TEM (HRTEM) image shows an interlayer spacing of 0.850 nm (Figure 2d), which corresponds to the (002) lattice crystal plane of CaVO and is in good agreement with the XRD results. In addition, it is observed from the energy dispersive spectrometer (EDS) mapping (Figure 2e) that Ca, V, and O are uniformly distributed in the nanoribbons, which further reflects the successful preparation of CaVO.

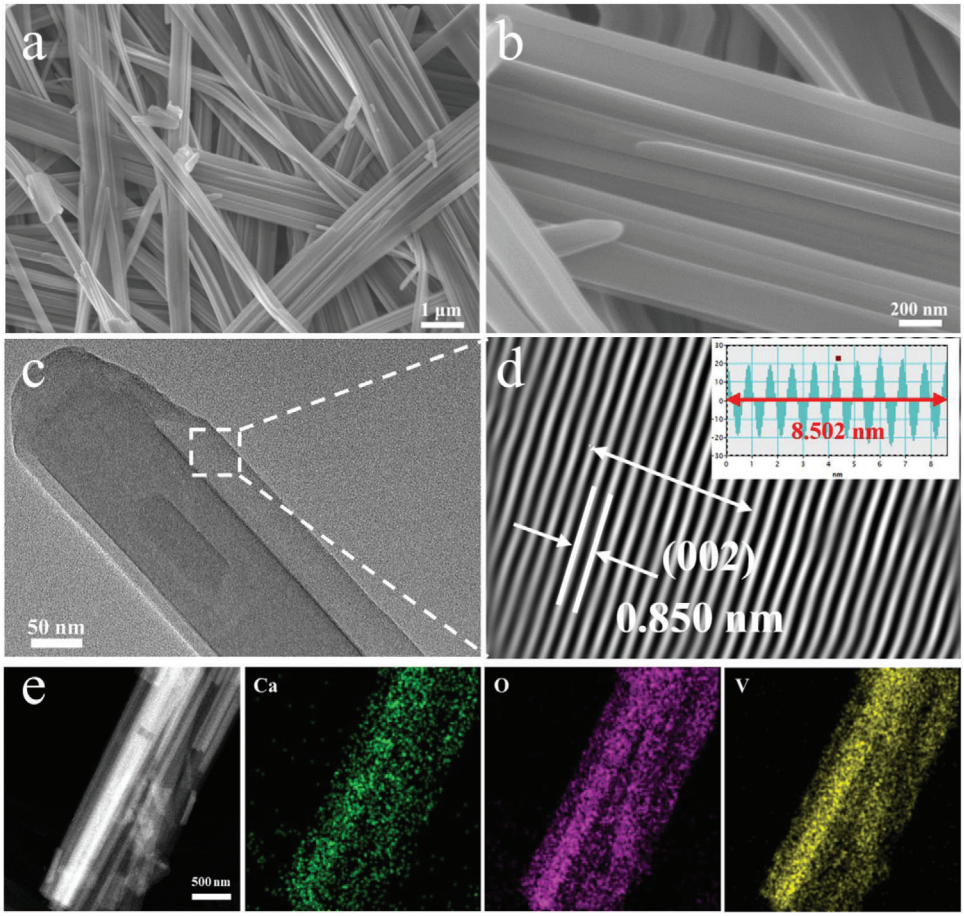


**Figure 2.** a,b) SEM images, c) TEM image, and d) HRTEM image of CaVO. e) TEM image of CaVO, and corresponding EDS elemental mapping of Ca, O, and V, respectively.

### 2.2. Electrochemical Properties

To evaluate the electrochemical performance of CaVO as cathode material in aqueous zinc metal batteries, coin cells were assembled employing Zn foil and 3 M $Zn(CF_3SO_3)_2$ as anode and electrolyte, respectively. **Figure** 3a depicts the cyclic voltammetry (CV) curves of the cell at a scan rate of 0.1 mV $s^{-1}$. Two pairs of distinct redox peaks (0.97/0.72 V and 0.65/0.46 V) can be observed, suggesting a multistep de-/intercalation behavior in the electrolyte. The cells were subjected to galvanostatic dis-/charge to evaluate the specific capacity. Figure 3b displays the dis-/charge profiles at 0.1 A $g^{-1}$. All four dis-/charge profiles exhibit identical shapes and specific capacities. Two pairs of voltage plateaus can be observed, which correspond to the two pairs of redox peaks in the CV curves. In addition, the rate capability of the cells was tested with galvanostatic dis-/charge at various specific current rates. The dis-/charge profiles at the different current rates are shown in Figure 3c, and the obtained specific capacity is summarized in Figure 3d. At 0.05, 0.1, 0.2, 0.3, 0.4, 0.5, 0.7, 1, 1.25, 1.5, 1.75, and 2 A $g^{-1}$, the discharge specific capacity was 379, 341, 306, 282, 268, 256, 233, 206, 182, 163, 147, and 131 mAh $g^{-1}$, respectively. When the specific current was returned to 0.5 A $g^{-1}$, the CaVO cathode was still able to deliver a discharge-specific capacity of 250 mAh $g^{-1}$, corresponding to 97.7% of the initial capacity at 0.5 A $g^{-1}$. Based on the GITT performed at 0.05 A $g^{-1}$ (Figure S4, Supporting Information), the calculated diffusion coefficient for the intercalating species is in the range of $10^{-9}$ to $10^{-10}$ $cm^2$ $s^{-1}$. The cycling stability of CaVO was evaluated via long-term dis-/charge cycling at 0.2 A $g^{-1}$ after three activation cycles at 0.05 A $g^{-1}$. The evolution of specific capacity and Coulombic efficiency upon the test is displayed in Figure 3e, and the dis-/charge profiles at a few selected cycles are shown in Figure 3f. After 500 cycles, its capacity retention was 88.5%, demonstrating the high cyclability of the prepared CaVO as a cathode material for aqueous zinc metal batteries. The cyclability was further tested at an elevated specific current (1 A $g^{-1}$). Impressively, the CaVO cathode offered a capacity retention of 94.4% after 2200 cycles. The regular fluctuations of the specific capacity observed in Figure 3g are caused by the changes in ambient temperature over the 24 h period.[19] For example, the cell underwent 73 charge/discharge cycles between the first and second peaks, taking ≈24 h. This behavior was, in fact, periodically observed in the subsequent cycling. The ambient temperature affects the ionic conductivity of the electrolyte and the electrochemical activity of the electrode materials.[24] Specifically, lower temperatures result in capacity reduction. As a result, the cell exhibited higher specific capacity during the day compared to the night. Additionally, it is noticed that the different current

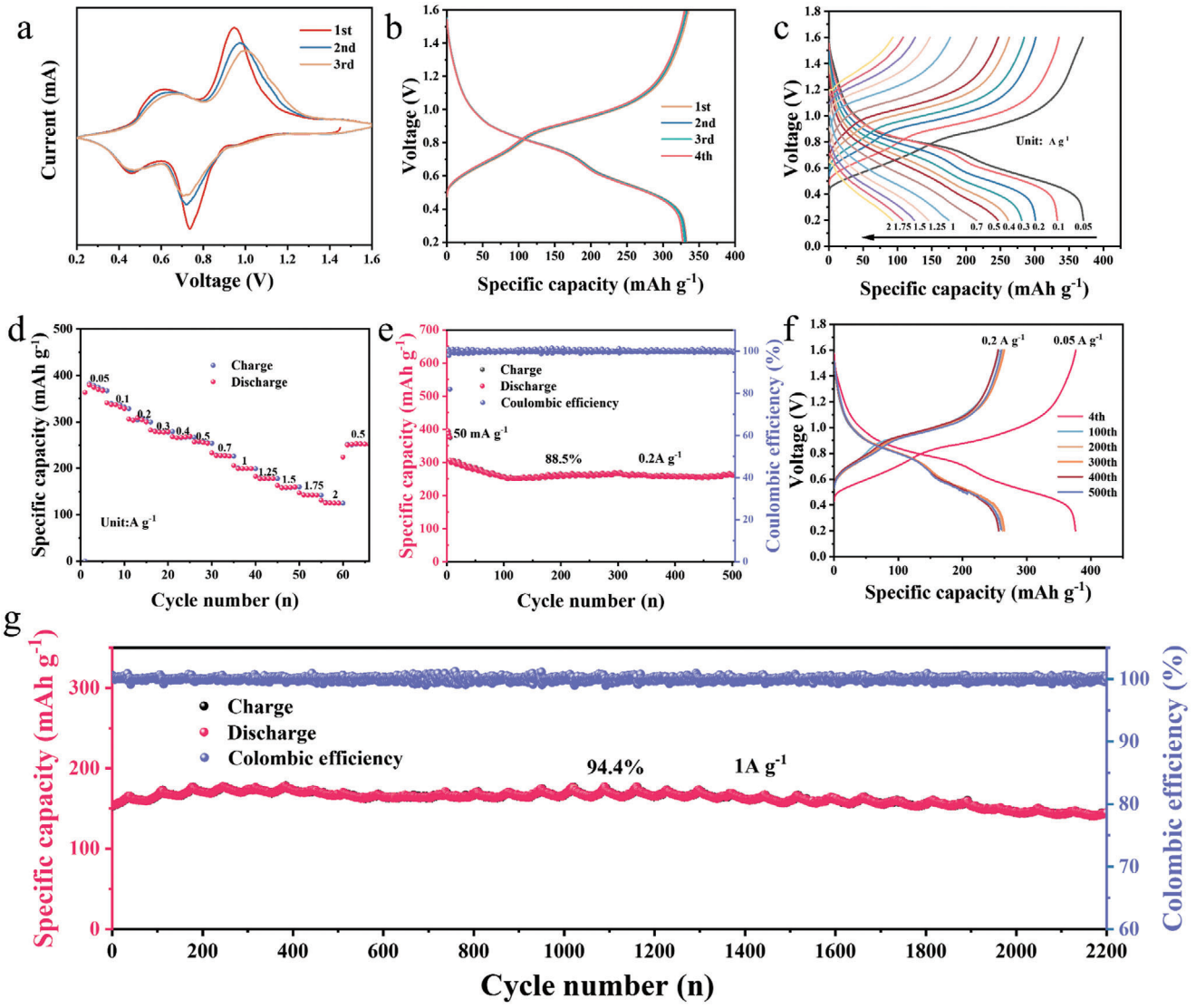


**Figure 3.** Electrochemical performance of CaVO as a cathode in aqueous zinc metal batteries. a) CV curves at 0.1 mV $s^{-1}$ sweep rate. Galvanostatic dis-/charge profiles b) in the initial 4 cycles at 0.1 A $g^{-1}$ and c) increasing specific current rates from 0.05 to 2.0 A $g^{-1}$. d) Evolution of specific capacity upon the rate capability test. Evolution of specific capacity and Coulombic efficiency upon the cyclability test at e) 0.2 A $g^{-1}$ and g) 1.0 A $g^{-1}$. f) The dis-/charge profiles at a few selected cycles upon the cyclability test at 0.2 A $g^{-1}$.

rates affect the capacity evolution trend in early cycling. At low specific current, the high number of ions intercalated into CaVO leads to a more pronounced reorganization of the electrode material, leading to the observed capacity decrease in the initial cycles (Figure 3e). At higher specific current, e.g., 1 A $g^{-1}$ (Figure 3g), the cell exhibits lower specific capacity, i.e., fewer guest ions are intercalated into CaVO. This weakens the extent of the active material's reorganization and its effect on specific capacity. Additionally, the electrode applied with a high specific current exhibits higher polarization and nonuniform diffusion of the intercalated ions, which results in the poor utilization of the active material during the initial cycles. However, as cycling progresses, these issues gradually reduce, which increases specific capacity in the early cycles. Nonetheless, these results indicate that CaVO exhibits excellent cyclability under both high and low specific currents. Table S2 (Supporting Information) presents a comparison of various vanadium-based cathode materials, encompassing the synthesis method and corresponding conditions and the electrochemical performance. It is observed that the synthesis herein reported has a significant advantage over the others from the facile and yield point of view. Despite the preparation at this large batch, the prepared CaVO exhibits promising electrochemical performance.

In a further step, we increased the mass loading from 1.5–2.0 to 6 mg $cm^{-2}$. After two activation cycles at 100 mA $g^{-1}$ (0.6 mA $cm^{-2}$), the cell tested at 0.3 A $g^{-1}$ delivered 251 mAh $g^{-1}$ (**Figure 4a**), corresponding to an areal capacity of 1.51 mAh $cm^{-2}$, at a current density of 1.8 mA $cm^{-2}$. After 100 cycles, 92.7% of the initial capacity was still delivered. The dis-/charge profiles of a few selected cycles are displayed in Figure 4b. The raw material,

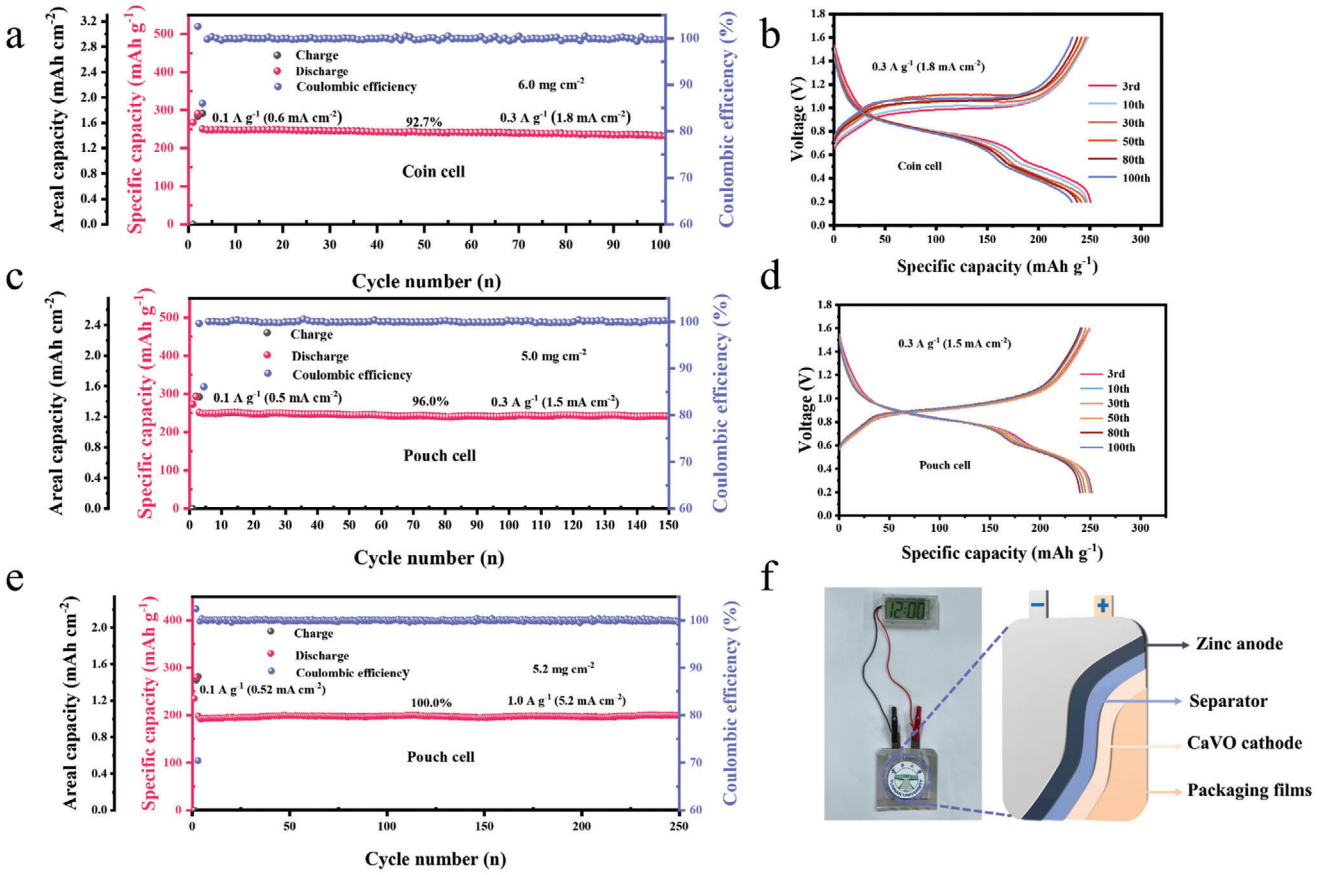


**Figure 4.** Electrochemical performance of high loading CaVO cathodes in coin cells and pouch cells. a) Evolution of specific capacity, areal capacity, and Coulombic efficiency upon the cyclability test at 0.3 A g$^{-1}$ of a Zn/CaVO coin cell. b) Dis-/charge profiles at a few selected cycles upon the cyclability test at 0.3 A g$^{-1}$ of the coin cell. Evolution of specific capacity, areal capacity, and Coulombic efficiency upon the cyclability test at c) 0.3 A g$^{-1}$ and e) 1.0 A g$^{-1}$ of pouch cells after two formation cycles at 0.1 A g$^{-1}$. d) Dis-/charge profiles of the of pouch cell at a few selected cycles upon the cyclability test at 0.3 A g$^{-1}$. f) Photograph of the pouch cell powering an electronic watch and the schematic illustration the pouch cell.

i.e., $V_2O_5$, for the preparation of CaVO was also tested with the same test protocol. As displayed in Figure S5 (Supporting Information), $V_2O_5$ exhibited only 41 mAh g$^{-1}$ at 0.3 A g$^{-1}$. These results further demonstrate the potential application of CaVO material at large loading and highlight a notable performance advantage over $V_2O_5$.

CaVO electrodes with areal loading of 5.0–5.2 mg cm$^{-2}$ were further used to assemble single-layer pouch cells. After two formation cycles at 0.1 A g$^{-1}$ (0.5 mA cm$^{-2}$), a pouch cell was dis-/charged at 0.3 A g$^{-1}$ (1.5 mA cm$^{-2}$), delivering 251 mAh g$^{-1}$ (i.e., as for the coin cell test) with 96.0% capacity retention after 150 cycles (Figure 4c). A few selected galvanostatic dis-/charge cycle profiles at 0.3 A g$^{-1}$ are provided in Figure 4d. The cyclability was further tested at an elevated specific current (1 A g$^{-1}$), and the results are displayed in Figure 4e. Notably, 198 mAh g$^{-1}$ was delivered at 1.0 A g$^{-1}$ (5.2 mA cm$^{-2}$) with no capacity fading after 250 cycles. In addition, the prepared pouch cell is capable of successfully powering an electronic watch (Figure 4f). The electrochemical behavior at this high areal mass loading and in the pouch cell configuration demonstrates the potential use of CaVO electrode material for practical application.

The promising cyclability of the prepared CaVO, particularly with respect to the $V_2O_5$ raw material, can be attributed to the high structural stability endowed by the $Ca^{2+}$ in the V-O interlayer.[25] Inductively Coupled Plasma Optical Emission Spectrometer (ICP-OES) was employed to analyze the molar ratios of V to Ca of the electrode material after different dis-/charge cycles. The content of Ca in pristine $Ca_xV_6O_{16}$ and after 1, 10, and 100 cycles were measured to be 1.09, 0.89, 0.71, and 0.71, respectively. During the cycling process from the 1st to the 10th cycle, x decreased from 0.89 to 0.71, indicating a slight leaching of $Ca^{2+}$. However, by the 100$^{th}$ cycle, the value of x remained at 0.71. Therefore, ≈65% of the pristine $Ca^{2+}$ still presents in the interlayer of CaVO, contributing to the stabilization of the crystal structure even upon long-term dis-/charge cycling. Additionally, the qualitative dissolution of CaVO and $V_2O_5$ in the electrolyte was tested (Figure S3, Supporting Information). Specifically, 0.05 g CaVO or 0.05 g $V_2O_5$ were added into 5 mL of the 3 M $Zn(CF_3SO_3)_2$ aqueous electrolyte. After 14 days, the electrolyte contacting $V_2O_5$ changed from colorless to yellow, demonstrating the leaching of vanadium, while the electrolyte contacting CaVO was still colorless. These results demonstrate that CaVO has a lower solubility than $V_2O_5$ in the electrolyte.

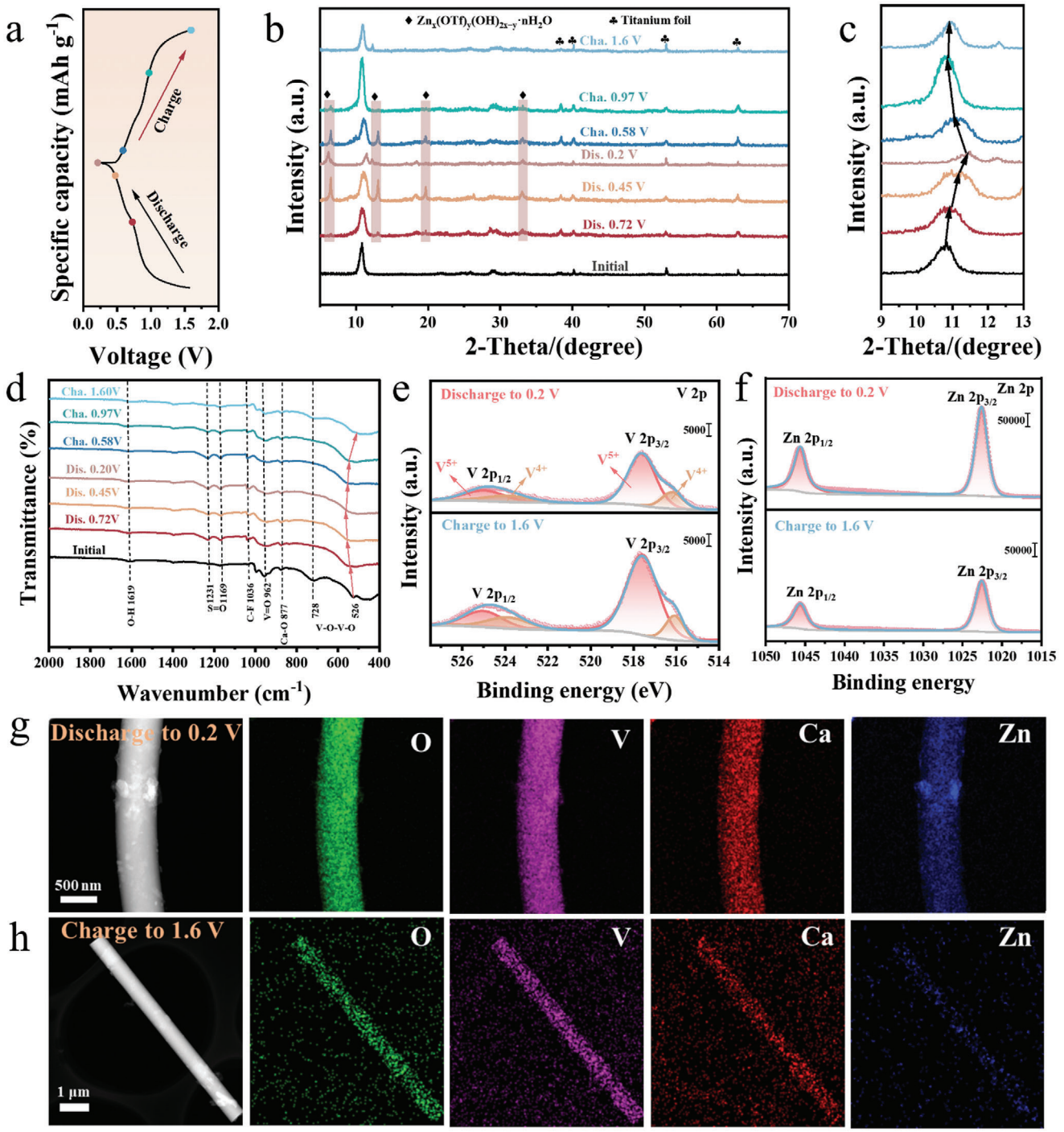


**Figure 5.** (a) Typical dis-/charge profile at 0.1 A $g^{-1}$ of the electrodes further subjected to ex-situ XRD. (b,c) Ex-situ XRD patterns and (d) ex-situ FTIR spectra of CaVO electrodes at various states of charge in the first cycle. High-resolution (e)V 2p and (f) Zn 2p XPS spectra of fully charged and discharged CaVO electrodes. TEM image of CaVO (g) fully discharged and (h) fully charged states and corresponding EDS elemental mapping of Ca, O, and V, respectively.

### 2.3. Energy Storage Mechanism

To investigate the energy storage mechanism of CaVO, some series of ex situ characterizations were carried out toward CaVO electrodes at different states of charge in the initial dis-/charge cycle at 0.1 A $g^{-1}$. The crystal structure evolution of the electrodes was first characterized with ex situ XRD, and the results are shown in **Figure** 5a–c. When the electrode is discharged to a voltage below 0.72 V, a series of new diffraction peaks at 6.4°, 13.0°, 19.6°, and 33.1° can be observed, which corresponds to

a layered double hydroxide (BZS), i.e., $Zn_x(OTf)_y(OH)_{2x-y}\cdot nH_2O$ accordingly to the previous literature.[26] Notably, the diffraction peaks of $Zn_x(OTf)_y(OH)_{2x-y}\cdot nH_2O$ exhibited a slight shift for the different samples, which can be ascribed to the change of the chemical formula, e.g., x, y, and n. In particular, the drying process during the sample preparation could change the amount of water (n) in the interlayer, thereby altering the interlayer distance and the diffraction peaks. Since this compound originates from the precipitation reaction between $Zn(CF_3SO_3)_2$ and $OH^-$, it is considered an indicator of increased local pH value due to the intercalation of $H^+$ into CaVO.[27] Figure S6 (Supporting Information) displays the SEM images of the fully discharged electrode. As it can be seen, the electrode surface is fully covered with the generated BZS byproducts. On the contrary, upon the charge, these new diffraction peaks show decreasing intensity along with the increase of the charging depth and almost disappear at the fully charged state (1.6 V). This indicates the disappearance of the BZS byproduct, which is also visualized in the SEM image of the fully charged electrode (Figure S7, Supporting Information). The formation and disappearance of the BZS upon discharge and charge, respectively indicate for the reversible intercalation and de-intercalation of $H^+$ in CaVO with this electrolyte.

In addition to the BZS phase, the shift of the (002) crystalline plane feature of CaVO is also observed during the dis-/charge processes, as displayed in Figure 5c. During discharge, the peak gradually shifted to higher $2\theta$, indicating the decrease of the interlayer distance, which can be attributed to the strong electrostatic attraction between the intercalated guested ions and the negatively charged $(V_6O_{16})^{2-}$ layer.[28] This peak then shifted back to lower $2\theta$ values during the subsequent charge and returned to the initial position at the fully charged state, indicating the recovery of the interlayer distance upon charge. This reversible change of the peak position and the interlayer spacing confirms the reversibility and flexibility of the CaVO crystal structure upon the dis-/charge processes.

Ex situ FTIR was used to further investigate the structural changes of the CaVO cathode during the initial dis-/charge cycle (Figure 5d). The intensity of S = O (at 1231 and 1169 $cm^{-1}$) and C-F (1036 $cm^{-1}$) peaks were significantly enhanced during discharge,[29] which is associated with the generation of BZS at the electrode surface. After a charge, all the characteristic peaks are almost restored to the same state as the original peaks, corresponding to the decomposition of BZS, which is consistent with the ex situ XRD resuts. It is worth noting that ion intercalation usually leads to an increase in the intra-layer stress, which is also confirmed with ex situ FTIR.[30] For example, the band at 526 $cm^{-1}$ belongs to a V-O-V-O chain with a laminar structure, which gradually moves to higher wavenumbers during the discharge, indicating an increase in the intra-layer stress upon intercalation of the guest ions. In contrast, the peak gradually moves to lower wavenumbers during charge, finally returning to the initial position at the fully charged state. This corresponds to the release of the intra-layer stress after the guest ions are de-intercalated from CaVO. These results once again demonstrate the reversible intercalation process in the synthesized CaVO.

Ex situ XPS was also conducted on CaVO electrodes at the fully discharged and charged states. Figure 5d displays the V 2p XPS spectra. The signals originating from both $V^{5+}$ and $V^{4+}$ are observed from both the fully charged and fully discharged electrodes. The peak area ratio between $V^{5+}$ and $V^{4+}$ is higher for the fully charged CaVO electrode (7.4) with respect to the fully discharged CaVO electrode (5.7), which indicates that some of the $V^{5+}$ ions are reduced to $V^{4+}$ upon discharge. The Zn 2p high-resolution XPS spectra of the electrodes are shown in Figure 5f. Since the generated BZS contains zinc, it is not possible to know whether the signal observed in the fully discharged sample receives the contribution from the $Zn^{2+}$ intercalated into CaVO. Nonetheless, the fully charged sample also shows a distinguished signal in the Zn 2p high-resolution XPS spectra, which can be attributed to residual $Zn^{2+}$ intercalated into CaVO as the previous interference phase, i.e., BZS, is not present at the fully charged state (Figure 5b and Figure S7, Supporting Information).[31] This result demonstrates the occurrence of $Zn^{2+}$ de-/intercalation for the CaVO electrode in aqueous zinc metal batteries.

TEM images of CaVO particles of fully discharged and charged electrodes are shown in Figure S8 (Supporting Information). It is observed that the intercalation and de-intercalation of $Zn^{2+}$ and $H^+$ do not change the micro-morphology of CaVO (Figure S8a,c, Supporting Information). The HRTEM images of the CaVO particle at the fully discharged state (Figure S8b, Supporting Information) show a slight contraction of the ($\bar{4}06$) plane (from initial 2.628 to 2.602 Å). For the fully charged sample, the lattice spacing recovers to 2.622 Å (Figure S8d, Supporting Information). The lattice breathing observed from the HRTEM images is consistent with the ex situ XRD results, which demonstrate the reversible de-/intercalation process during the dis-/charge cycle. The EDS mapping images of the CaVO particles from the electrodes at the fully discharged and fully charged states are shown in Figure 5g,h. The uniform distribution of Ca, V, and O matches well with the TEM images. Particularly, the presence of Ca in the fully charged state indicates that the $Ca^{2+}$ ions in the interlayer are not released upon charge and therefore function as pillars stabilizing the structure of the material. For the fully discharged sample, some parts of the CaVO particle show a strong Zn signal, which could be from the generated BZS. Even though, the Zn signal is also observed throughout the entire CaVO particle, which implies intercalation of $Zn^{2+}$. More solid evidence of $Zn^{2+}$ intercalated into CaVO is given by the fully charged sample, as the Zn signal is still observed (Figure 5h) while BZS is not present in this electrode. Nonetheless, the Coulombic efficiency of the dis-/charge cycle reaches 99.6%, indicating that the irreversible process is very limited. This result is consistent with the XPS results of the CaVO electrodes.

### 2.4. DFT Theoretical Calculations

The previous experimental results demonstrate a high structural stability of CaVO upon repeated electrochemical de-/intercalation. This could be related to the $Ca^{2+}$ ions in the interlayer, as it has been reported that the pillar agent in the interlayers can weaken the electrostatic interactions between the $[VO_n]$ layer and $Zn^{2+}$.[32] To study the effect of $Ca^{2+}$ as the pillar agent on the kinetics of $Zn^{2+}$ ion diffusion, density-functional theory (DFT) calculations were conducted. As shown in **Figure 6a**, $Ca^{2+}$ is found to generate Van der Waals forces through hydrogen bonding with lattice oxygen and water molecules, elucidating the strong bonding between the V-O layer and $Ca^{2+}$ as well as the

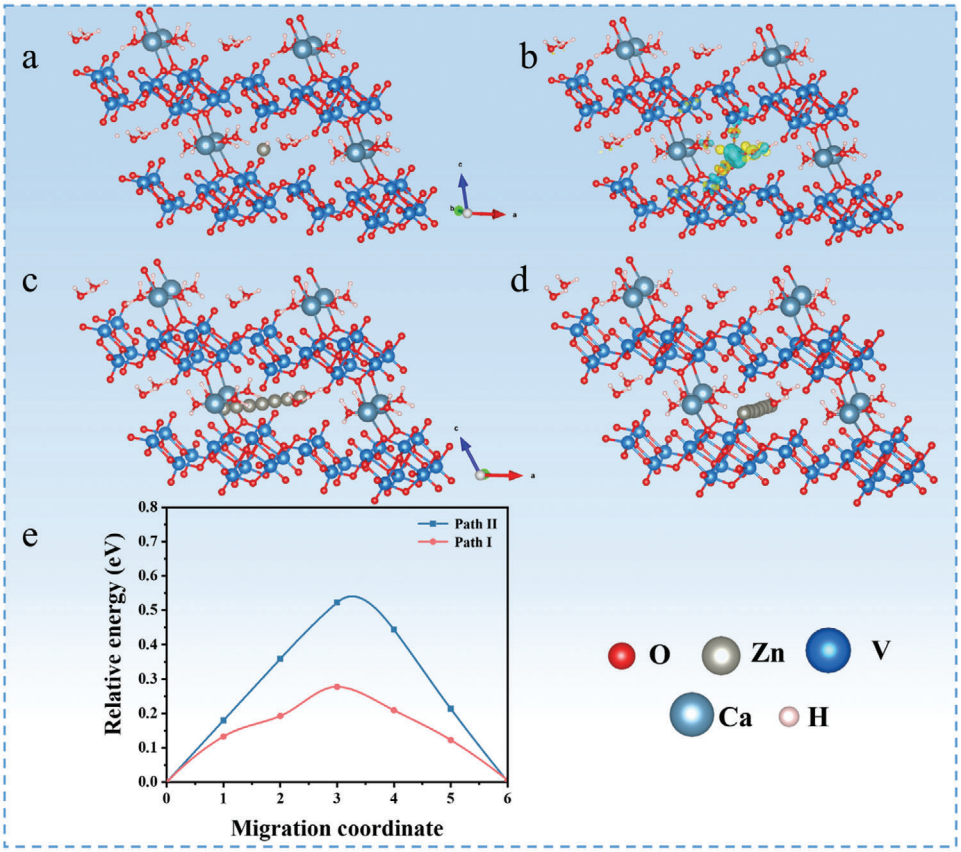


**Figure 6.** a) Structural diagram of $Zn^{2+}$ inserted in the CaVO structure. b) Differential charge densities of inserted $Zn^{2+}$ in CaVO c,d) Simulated diffusion paths of $Zn^{2+}$ along the *a*- and *b*-axis in CaVO, and e) diffusion energy barriers of $Zn^{2+}$ along the two paths (*a*- and *b*-axis).

enlarged layer spacing. The differential charge density analysis when a single $Zn^{2+}$ is inserted into the layered structure is shown in Figure 6b. The yellow region indicates the accumulation of electrons, and the blue region indicates the depletion of electrons (0.002 eV $Å^{-3}$ for the equivalent face value). Calculations show that CaVO has an off-domain electron cloud, which helps to promote charge transfer kinetics and thus improves the reversibility of the cell during deep cycling.[29] To further understand the diffusion path of $Zn^{2+}$ into the material, simulations were performed based on the lattice structure properties of CaVO. The diffusion paths of $Zn^{2+}$ migration between the $V_3O_8$ layers of CaVO, along the *a*-axis (path I) and *b*-axis (path II) are shown in Figure 6c,d, respectively. Subsequently, the diffusion potential barriers of $Zn^{2+}$ in CaVO were further calculated along these two paths. As displayed in Figure 6e, $Zn^{2+}$ tends to diffuse along the *a*-axis in CaVO with a low energy barrier of 0.27 eV.

## 3. Conclusion

Phase-pure CaVO has been successfully prepared at mild temperature via an effective and efficient "oil bath" method. With commercial crystalline $V_2O_5$, $Ca(CH_3COO)_2$, and water as the raw materials, phase-pure CaVO with 42.8 g per batch and a yield of 98.8% can be obtained via facile oil-bath heating the reactant at 90 °C for 6 h, which offers significant advantages over previous preparation procedures in terms of simplicity, time, and cost reduction. The physical and electrochemical investigation indicates that pre-intercalated $Ca^{2+}$ ions and $H_2O$ not only significantly widen the layer spacing, but also stabilize the crystal structure. In addition, DFT calculations show that the introduction of $Ca^{2+}$ and $H_2O$ can weaken the electrostatic interactions between $Zn^{2+}$ and the V-O layer, thus effectively improving the diffusion kinetics of $Zn^{2+}$. DFT theoretical calculations reveal that $Ca^{2+}$ can modulate the migration of $Zn^{2+}$. Based on these advantages, the CaVO cathode exhibits a high specific capacity (379 mAh $g^{-1}$ at 0.05 A $g^{-1}$) and excellent long-term cyclability (94.4% capacity retention after 2200 cycles at a current density of 1 A $g^{-1}$). These results suggest that CaVO materials can be competitive cathode candidates for AZMBs. In addition, this synthesis strategy, which offers great advantages in terms of time and cost, will hopefully be extended to the synthesis of other vanadium-based materials as well.

## Supporting Information

Supporting Information is available from the Wiley Online Library or from the author.

## Acknowledgements

M.L. and X.L. contributed equally to this work. The authors would like to show gratitude to the Yunnan Key Laboratory of Carbon Neutrality and

Green Low-Carbon Technologies (No. 202205AG070002 (Y.W.)), the National Natural Science Foundation of China (No. 61761047 and 41876055 (Y.W.)), and the Program for Innovative Research Team (in Science and Technology) in University of Yunnan Province, the Project of the Department of Education of Yunnan Province (2023Y0263), and the Yunnan University's Research Innovation Fund for Graduate Students (KC-23234583) and (KC-23234550). Financial support from the Helmholtz Association is acknowledged.

Open access funding enabled and organized by Projekt DEAL.

## Conflict of Interest

The authors declare no conflict of interest.

## Data Availability Statement

The data that support the findings of this study are available on request from the corresponding author. The data are not publicly available due to privacy or ethical restrictions.

## Keywords

aqueous zinc batteries, cathode material, $CaV_6O_{16}$, effective preparation, vanadium oxide

Received: September 4, 2024
Revised: November 17, 2024
Published online:

[1] a) P. Liang, K. Zhu, Y. Rao, Z. Kong, J. Chen, H. Zheng, J. Liu, K. Yan, J. Wang, K. Zeng, *ACS Appl. Mater. Interfaces* **2024**, *16*, 24723; b) D. Zhang, W. Wang, S. Li, X. Shen, H. Xu, *Energy Storage Mater.* **2024**, *69*, 3436; c) A. Song, Z. Dan, S. Zheng, Y. Zhou, *Nat. Commun.* **2024**, *15*, 5905.

[2] N. Kittner, F. Lill, D. M. Kammen, *Nat. Energy* **2017**, *2*, 17125.

[3] a) S. Deng, B. Xu, J. Zhao, H. Fu, *Energy Storage Mater.* **2024**, *70*, 3490; b) W. Ma, S. Wang, X. Wu, W. Liu, F. Yang, S. Liu, S. C. Jun, L. Dai, Z. He, Q. Zhang, *Energy Environ. Sci.* **2024**, *17*, 4819; c) J. Zhu, Z. Tie, S. Bi, Z. Niu, *Angew. Chem. Int. Ed. Engl.* **2024** ,*63*, 202403712; d) H. Liu, X. Hou, T. Fang, X. Luo, Y. Li, X. Hu, Z. Chen, Y. Li, W. Peng, X. Fan, *Energy Storage Mater.* **2024**, *65*, 3092.

[4] a) Y. Dai, C. Zhang, J. Li, X. Gao, P. Hu, C. Ye, H. He, J. Zhu, W. Zhang, R. Chen, W. Zong, F. Guo, I. P. Parkin, D. J. L. Brett, P. R. Shearing, L. Mai, G. He, *Adv. Mater.* **2024**, *36*, 2310645; b) Q. Wang, J. Wu, M. Wang, H. Yu, X. Qiu, W. Chen, *Adv. Sci.* **2024**, *11*, 2307872.

[5] a) X. Chen, J.-H. Liu, H. Jiang, C. Zhan, Y. Gao, J. Li, H. Zhang, X. Cao, S. Dou, Y. Xiao, *Energy Storage Mater.* **2024**, *65*, 3168; b) X. Shi, C. Zhou, F. Yang, L. Shan, B. Tang, J. Zhang, Q. Nan, Y. Xie, J. Li, H. Li, X. Tian, *ACS Energy Lett.* **2024**, *9*, 1063; c) F. Zhao, J. Li, A. Chutia, L. Liu, L. Kang, F. Lai, H. Dong, X. Gao, Y. Tan, T. Liu, I. P. Parkin, G. He, *Energy Environ. Sci.* **2024**, *17*, 1497.

[6] a) L. Ye, H. Fu, R. Cao, J. Yang, *J. Colloid Interface Sci.* **2024**, *664*, 423; b) Z. Song, L. Miao, H. Duan, Y. Lv, L. Gan, M. Liu, *Angew. Chem. Int. Ed.* **2024**, *63*, 202401049.

[7] a) D. Li, Y. Guo, C. Zhang, X. Chen, W. Zhang, S. Mei, C.-J. Yao, *Nano-Micro Lett.* **2024**, *16*, 194; b) B. Niu, J. Wang, Y. Guo, Z. Li, C. Yuan, A. Ju, X. Wang, *Adv. Energy Mater.* **2024**, *14*, 2303967; c) Q.-Q. Sun, T. Sun, J.-Y. Du, K. Li, H.-M. Xie, G. Huang, X.-B. Zhang, *Adv. Mater.* **2023**, *35*, 2301088.

[8] a) Q. He, T. Hu, Q. Wu, C. Wang, X. Han, Z. Chen, Y. Zhu, J. Chen, Y. Zhang, L. Shi, X. Wang, Y. Ma, J. Zhao, *Adv. Mater.* **2024**, *36*, 2400888; b) X. Wang, Y. Wang, A. Naveed, G. Li, H. Zhang, Y. Zhou, A. Dou, M. Su, Y. Liu, R. Guo, C. C. Li, *Adv. Funct. Mater.* **2023**, *33*, 2306205.

[9] a) X. Dou, X. Xie, S. Liang, G. Fang, *Sci. Bull.* **2024**, *69*, 833; b) Z. Wang, Y. Song, J. Wang, Y. Lin, J. Meng, W. Cui, X.-X. Liu, *Angew. Chem. Int. Ed.* **2023**, *62*, 16290.

[10] a) G. Shi, P. Zhao, P. Gao, Y. Xing, B. Shen, *J. Energy Storage* **2024**, *78*, 110057; b) Y. Bai, Y. Qin, J. Hao, H. Zhang, C. M. Li, *Adv. Funct. Mater.* **2024**, *34*, 2310393; c) Y. Xu, G. Fan, P. X. Sun, Y. Guo, Y. Wang, X. Gu, L. Wu, L. Yu, *Angew. Chem. Int. Ed.* **2023**, *62*, 202303529.

[11] D. Kundu, B. D. Adams, V. Duffort, S. H. Vajargah, L. F. Nazar, *Nat. Energy* **2016**, *1*, 16119.

[12] a) F. Jing, Y. Liu, Y. Shang, C. Lv, L. Xu, J. Pei, J. Liu, G. Chen, C. Yan, *Energy Storage Mater.* **2022**, *49*, 164; b) C. Zhang, Y. Huang, X. Xu, Z. Chen, G. Xiao, Y. Zhong, X. Wang, C. Gu, J. Tu, *Energy Environ. Sci.* **2024**, *17*, 4090; c) T. Lv, G. Zhu, S. Dong, Q. Kong, Y. Peng, S. Jiang, G. Zhang, Z. Yang, S. Yang, X. Dong, H. Pang, Y. Zhang, *Angew. Chem. Int. Ed.* **2023**, *62*, 202216089; d) T. Zhou, L. Xie, Q. Han, X. Qiu, Y. Xiao, X. Yang, X. Liu, S. Yang, L. Zhu, X. Cao, *Coord. Chem. Rev.* **2024**, *498*, 215461; e) Y. Liu, C. Lu, Y. Yang, W. Chen, F. Ye, H. Dong, Y. Wu, R. Ma, L. Hu, *Adv. Mater.* **2024**, *36*, 2312982.

[13] M. Yan, P. He, Y. Chen, S. Wang, Q. Wei, K. Zhao, X. Xu, Q. An, Y. Shuang, Y. Shao, K. T. Mueller, L. Mai, J. Liu, J. Yang, *Adv. Mater.* **2018**, *30*, 1703725.

[14] a) T.-F. Yi, L. Qiu, J.-P. Qu, H. Liu, J.-H. Zhang, Y.-R. Zhu, *Coord. Chem. Rev.* **2021**, *446*, 214124; b) L. Kou, Y. Wang, J. Song, T. Ai, W. Li, P. Wattanapaphawong, K. Kajiyoshi, *Green Chem.* **2024**, *26*, 1709; c) G. Li, L. Sun, S. Zhang, C. Zhang, H. Jin, K. Davey, G. Liang, S. Liu, J. Mao, Z. Guo, *Adv. Funct. Mater.* **2024**, *34*, 2301291.

[15] a) Y. Bai, H. Zhang, B. Xiang, Y. Zhou, L. Dou, G. Dong, *J. Colloid Interface Sci.* **2021**, *597*, 422; b) J. Zhou, L. Shan, Z. Wu, X. Guo, G. Fang, S. Liang, *Chem. Commun.* **2018**, *54*, 4457.

[16] a) S. Cao, Y. Xiang, Q. Zou, Y. Jiang, H. Zeng, J. Li, J. Wu, X. Wu, X. Wu, L. Xiong, *RSC Adv.* **2023**, *13*, 24385; b) D. Bokov, A. Turki Jalil, S. Chupradit, W. Suksatan, M. Javed Ansari, I. H. Shewael, G. H. Valiev, E. Kianfar, *Adv. Mater. Sci. Eng.* **2021**, *2021*, 5102014.

[17] a) K. Zhu, T. Wu, K. Huang, *Chem. Mater.* **2021**, *33*, 4089; b) J. Wang, J. Wang, Y. Jiang, F. Xiong, S. Tan, F. Qiao, J. Chen, Q. An, L. Mai, *Adv. Funct. Mater.* **2022**, *32*, 2113030.

[18] a) K. Zhu, T. Wu, K. Huang, *ACS Nano.* **2019**, *13*, 14447; b) J. Livage, *Coord. Chem. Rev.* **1998**, *178–180*, 999.

[19] H. Liu, X. Hou, T. Fang, Q. Zhang, N. Gong, W. Peng, Y. Li, F. Zhang, X. Fan, *Energy Storage Mater.* **2023**, *55*, 279.

[20] D. Mueller, R. Hochleitner, K. T. Fehr, *J. Raman Spectrosc.* **2016**, *47*, 602.

[21] a) Y. Peng, L. e. Mo, T. Wei, Y. Wang, X. Zhang, Z. Li, Y. Huang, G. Yang, L. Hu, *Small* **2024**, *20*, 2306972; b) Q. Song, S. Zhou, S. Wang, S. Li, L. Xu, J. Qiu, *Chem. Eng. J.* **2023**, *461*, 142033; c) Z. Zhang, B. Xi, X. Wang, X. Ma, W. Chen, J. Feng, S. Xiong, *Adv. Funct. Mater.* **2021**, *31*, 2103070.

[22] X. Zhang, W. Yang, J. Liu, Y. Zhou, S. Feng, S. Yan, Y. Yao, G. Wang, L. Wan, C. Fang, Z. Zou, *Nano Energy* **2016**, *22*, 38.

[23] J. Yao, Y. Li, R. C. Masse, E. Uchaker, G. Cao, *Energy Storage Mater.* **2018**, *11*, 205.

[24] a) X. Yun, Y. Chen, H. Gao, D. Lu, L. Zuo, P. Gao, G. Zhou, C. Zheng, P. Xiao, *Adv. Energy Mater.* **2024**, *14*, 2304341; b) L. Jia, H. Hu, X. Cheng, H. Dong, H. Li, Y. Zhang, H. Zhang, X. Zhao, C. Li, J. Zhang, H. Lin, J. Wang, *Adv. Energy Mater.* **2023**, *14*, 2304010.

[25] a) Y. Zeng, S. Peng, X. Yang, Y. Dong, Q. Fan, Q. Kuang, Y. Zhao, *Chem. Eng. J.* **2023**, *478*, 147312; b) M. Du, F. Zhang, X. Zhang, W. Dong, Y. Sang, J. Wang, H. Liu, S. Wang, *Sci. China Chem.* **2020**, *63*, 1767.

[26] a) Y. Kim, Y. Park, M. Kim, J. Lee, K. J. Kim, J. W. Choi, *Nat. Commun.* **2022**, *13*, 2371; b) Y. Zhang, F. Wan, S. Huang, S. Wang, Z. Niu, J. Chen, *Nat. Commun.* **2020**, *11*, 2199; c) Z. Wang, Y. Zhang, H. Ye, H.

Cheng, X. Cai, M. Wei, Y. Gu, C. Liu, Y. Pan, D. Jia, H. Lin, *J. Energy Storage* **2024**, *83*, 110622.

[27] a) H. Liu, X. Hou, T. Fang, X. Luo, Y. Li, X. Hu, Z. Chen, Y. Li, W. Peng, X. Fan, *Energy Storage Mater.* **2024**, *65*, 103092; b) W. Liang, D. Rao, T. Chen, R. Tang, J. Li, H. Jin, *Angew. Chem. Int. Ed.* **2022**, *61*, 202207779; c) F. Wan, S. Huang, H. Cao, Z. Niu, *ACS Nano* **2020**, *14*, 6752.

[28] K. Zhu, W. Jiang, Z. Wang, W. Li, W. Xie, H. Yang, W. Yang, *Angew. Chem. Int. Ed.* **2023**, *62*, 202213368.

[29] Y. Ran, J. Ren, Z. C. Yang, H. Zhao, Y. Wang, Y. Lei, *Small Struct.* **2023**, *4*, 2300136.

[30] G. Yang, Q. Li, K. Ma, C. Hong, C. Wang, *J. Mater. Chem. A* **2020**, *8*, 8084.

[31] R. Cui, J. Gu, N. Wang, Y. Wang, X. Huang, S. Zhang, L. Lu, D. Wang, *Small* **2024**, *20*, 2307849.

[32] Q. Zong, Y. Zhuang, C. Liu, Q. Kang, Y. Wu, J. Zhang, J. Wang, D. Tao, Q. Zhang, G. Cao, *Adv. Energy Mater.* **2023**, *13*, 2301480.